I&EC research
Industrial & Engineering Chemistry Research

pubs.acs.org/IECR

Article

Thermal Decomposition Pathways of $Zn_xFe_{3-x}O_4$ Nanoparticles in Different Atmospheres

Published as part of "2022 Class of Influential Researchers".

Juliusz Kuciakowski,* Joanna Stępień, Jan Żukrowski, Dorota Lachowicz, Antoni Żywczak, Marta Gajewska, Marek Przybylski, Simone Pollastri, Luca Olivi, Marcin Sikora,* and Angelika Kmita*

Cite This: *Ind. Eng. Chem. Res.* 2022, 61, 12532−12544

Read Online

ACCESS | Metrics & More | Article Recommendations | Supporting Information

ABSTRACT: This article shows how initial composition and thermal treatment of nonstoichiometric zinc ferrite nanoparticles (nZFN) can be chosen to adjust the structure and cation distribution and enhance magnetism in the resulting nanoscale material. It also provides insight into new prospects regarding the production and design of nanoscale materials. Investigations were conducted before and after heating of nZFN in an inert atmosphere and a vacuum up to temperature of 1170 °C. Annealing leads to partial reduction of Fe ions, enhanced magnetism, and an increase in the size of the particles independent of the atmosphere. Use of the inert atmosphere delivers a solid solution of magnetite and zinc ferrite with a reduced Zn content in the structure as a result of sublimation of newly formed ZnO and reduction of Fe, and it favors crystallization. A preference for normal-spinel phase and enhancement of magnetic saturation from 20 Am^2/kg up to 101 Am^2/kg was observed. Vacuum annealing with high probability produces ZnO, Fe_3O_4, and Fe_2O_3 multiphase system with signs of amorphization, mainly on the surface. A large fraction of Fe ions is reduced and the volume ratio of Fe_3O_4 to Fe_2O_3 increases with heating time. The final solid product from a complete decomposition of ZFN is magnetite.

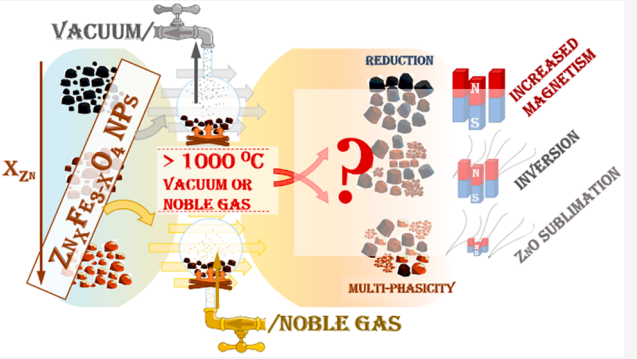

1. INTRODUCTION

1.1. Zinc Ferrite Nanoparticles in Spinel Structure Research. Comprehensive approach to design and synthesis of nanomaterials significantly widened possibilities of their application throughout vast life areas.[1−21] Nanoparticles with magnetic properties have been very interesting materials for basic research and technological applications for years.[22−26] The special attention of scientists is on ferrite nanoparticles with a spinel structure: $(M_{1-x}Fe_x)[M_xFe_{2-x}]O_4$, where the parentheses and square brackets denote the (tetrahedral) and [octahedral] sites (later Td and Oh, respectively), and M is a transition metal (for example, Zn, Mg, Co, or Fe). $ZnFe_2O_4$ nanoparticles (ZFN) are the subject of investigation, because of their unique magnetic properties, memory effect, superspin-glass ordering, low toxicity, specific microwave absorption, electrical properties, and photocatalytic activity.[4,7−9,14,23,26,27]

Ferrites of a spinel structure provide a possibility of controlling chemical and physical properties.[2,7,14,28] On the nanoscale, at room temperature (RT), ZFN reveal superparamagnetic response, while at a cryogenic temperature of −268 °C (∼5 K), they show ferrimagnetic properties.[9,25,29−31] Alterations are possibly caused by, e.g., the nanoparticle size, applied magnetic field, or dipole−dipole interactions.[15,16]

The magnetic, electronic, and optical properties of spinel ferrites all are dependent on changes in sizes and distributions of cations in the crystal lattice, from the bulk zinc ferrite (ZF), to the normal-inverse mixed spinel structure, characteristic for nanoparticles.[9,28,32−34] The magnitude of this effect is parametrized by the degree of inversion (σ) quantifying the distribution of M^{2+} and Fe^{3+} cations among Td and Oh sites, e.g., $(Zn_{1-\sigma}Fe_\sigma)[Zn_\sigma Fe_{2-\sigma}]O_4$ in perfectly normal spinel structure means $\sigma = 0$. σ is dependent on the relative sizes of cations, their charges, and the relative crystal-field stabilization offered by the tetrahedral or octahedral coordination.[28,35−38]

ZFN are widely used in several domains, e.g., in medicine as biosensors, as spin filters in spintronic, environment purification processes, and many more.[6,14,23,39−41] The above-mentioned applications are related mainly to operation in RT. However, they are fulfilling demands also in higher-temperature regimes,

Received: May 4, 2022
Revised: July 26, 2022
Accepted: July 27, 2022
Published: August 11, 2022

such as gas sensors, absorbents, and catalysts.[18−20,42,43] Recent investigations proved that the behavior of materials in nanoscale at high temperatures could widen their potential applications.[44−47] This effect is largely related to the surface enthalpy and activation energy. As an example in composite materials: rubber ZFN composite constitutes nanostrengthening,[48] which improves usable characteristics, such as thermal stability and mechanical properties. The spinel structure of ferrites gives wide possibilities of controlling their properties (e.g., magnetic) by changing the chemical composition (including variable Zn:Fe ratio). This creates a wide field for using nonstoichiometric ZFN (nZFN) in practical applications.[1,9,13,32] Because of an expanding field of ZFN application, we should take into consideration extreme conditions of high temperature, near and above their thermal decomposition temperature of ∼1200 °C (1473 K).[12,35,49−52]

Investigation of their properties at such high temperature seems essential. When a temperature influence on ZFN is discussed, the special attention should be directed at the temperature range and the type of atmosphere in which the process occurred, both of which have the potential to strongly alter the results, which is further explained below.

1.2. Zinc Ferrite Decomposition under Inert Conditions. Zinc ferrite is used for the production of O_2 and/or H_2 through the exploitation of solar energy.[53−57] Kaneko et al.[53] indicated that the thermal decomposition of zinc ferrite in an inert gas atmosphere started at a temperature above 1227 °C (1500 K), while at a temperature of 1477 °C (1750 K), its degree of decomposition was 40%. Temperature of the onset of decomposition equal to 1227 °C (1500 K) was reached after ∼40 s. As far as applications of ZF at high-temperature processes are concerned, studies on utilizing ZFN are performed only since recently, for example in the production of H_2 utilizing zinc ferrite in a form of nanorods or thin layers.[12,58]

1.3. Zinc Ferrite Nanoparticles Decomposition under Inert Conditions. Systematic investigations of the temperature influence on structural and magnetic changes occurring in nonstoichiometric zinc ferrite nanoparticles (nZFN) are discussed in the work of Kmita et al.[35] Samples were heated with a constant rate β = 10 °C/min up to 1400 °C, in an inert atmosphere. Investigations indicated that nZFN were undergoing the thermal decomposition from 20% to 24% in dependence on their degree of nonstoichiometry. Products formed after the heating of nanoparticles—ferrites with different compositions than initial samples—indicated high values of saturation magnetization (MS), of the order of 120 Am^2/kg, what was the effect of thermal decomposition and redistribution of cations in the spinel lattice.

1.4. Heating Zinc Ferrite Nanoparticles under Vacuum Conditions. Philip et al.[59] found that structure changes (of lattice constant a) and magnetic properties (increase in magnetization) occurred in ZFN after heating up to 1000 °C (1273 K) under vacuum conditions. The authors presented a belief that this is related to a redistribution of cations in the lattice, because of a high-temperature diffusion as well as a possible reduction of Fe^{3+} ions.[59]

Ayyappan et al.[60] indicated that ZFN annealed in a vacuum to 1000 °C (1273 K) become ferromagnetic, while these treated in air reveal paramagnetic properties. This indicates that a deficiency of oxygen during the annealing process is very important.

Investigations cited above, apart from the work of Kmita et al.,[35] concern ZF or ZFN of a stoichiometric composition. However, from the perspective of wide practical applications, there is a lack of results describing the influence of the type of annealing atmosphere on changes occurring in nZFN, e.g., which properties can be differently tuned. The investigation presented in this study aims at providing state-of-the-art knowledge concerning the thermal resistance of such nanomaterials. Literature review[9,61−68] proves that, in addition to classical analytical techniques, such as thermogravimetry, electron microscopy, magnetometry, and photoelectron spectroscopy, X-ray absorption spectroscopy (XAS) and Mössbauer spectroscopy are among the most suitable tools that allow one to test atomic and magnetic structures evolution occurring in nanoparticles, including ZFN. It makes selective sampling of ionization of the given element and categorization of its local surroundings possible. The spectra are sensitive to the degree of ion oxidation. In addition, their shape is strongly dependent on the chemical surroundings of the tested atoms, neighboring atoms, and distances and mutual angles of chemical bonds. There are two main regimes in the XAS: X-ray absorption near edge structure (XANES) spreading out from just before the edge to ∼40−50 eV behind the edge and extended X-ray absorption fine structure (EXAFS) starting above the XANES range and spreading toward much higher energies, even up to 1000 eV higher. XANES analysis allows one to determine the degree of oxidation of the given ion from placement of the absorption edge, while the shape of the spectrum provides information concerning the density of vacant electronic states. EXAFS measurements return information concerning the crystal lattice, mainly distances and types of the nearest neighbors of the analyzed element. From that information, it is possible to infer the positions—octahedral or tetrahedral—adopted by the given ions.[28]

1.5. Aim of Research. The aim of the research is to determine the effect of the type of atmosphere, temperature, and heating time on structural and magnetic changes occurring in stoichiometric and nonstoichiometric zinc ferrite nanoparticles.

2. EXPERIMENTAL SECTION

2.1. Materials. The subject of the research were $Zn_xFe_{3-x}O_4$ nanoparticles, where $x = x_{Zn}$ = 1.00, 0.86, or 0.35. Zinc ferrite nanoparticles of nonstoichiometric composition (nZFN) were produced by wet chemistry methods, and the conditions of their synthesis and properties were presented in our previous work.[35] nZFN ($Zn_xFe_{3-x}O_4$, $0 < x \leq 1$) were synthesized via coprecipitation and thermal methods in a nonaqueous solvent, which were redesignated.[35] In a typical coprecipitation process, adequate amounts of $FeCl_3{\cdot}6H_2O$, $FeCl_2{\cdot}4H_2O$, and $ZnCl_2$ were dissolved in deionized water (the ratio of the metal ions was Fe^{2+}:Fe^{3+}:Zn^{2+} = $(1 - x)$:2:x). A solution of $NaOH_{aq}$ was used as the precipitating agent.[35]

In a typical thermal method, $Fe(acac)_3$ and $Zn(acac)_2$ (molar ratio = 2:1) were dissolved in benzyl alcohol (which was used as the solvent, capping agent, and reducing agent). Next, the mixture was heated to 120 °C and kept for 1 h and finally heated to 200 °C to reflux the mixture and kept for 2 h.[35] The mixture with precipitates was cooled to ambient temperature and then washed by organic solvents (ethanol, diethyl ether) several times.[35] The dried samples in powder form were utilized for further investigations. The reference point was the commercially available (Sigma−Aldrich) ferrite nanoparticles with a stoichiometric composition (x_{Zn} = 1).

2.2. Methods. *2.2.1. Thermal Treatment.* The analyzed ZFN were subjected to high temperature in an inert atmosphere

https://doi.org/10.1021/acs.iecr.2c01572
Ind. Eng. Chem. Res. 2022, 61, 12532−12544

and vacuum, according to the following temperature regime: from 30 °C to 1000 °C at a rate of $\beta = 10$ °C/min, from 1000 °C to 1170 °C at $\beta = 1$ °C/min, and isothermal annealing for 10 min at a constant temperature of 1170 °C. The samples obtained in this way were the subject of further research. The Q600 (TA Instruments) thermal analyzer was used for simultaneous evaluation of the mass change (thermogravimetry analysis, TGA) and transformation energetics (differential scanning calorimetry, DSC) as a function of increasing temperature under inert atmosphere. For vacuum conditions, the samples were heated in a ceramic tube furnace at a base pressure equal to 5 mbar.

2.2.2. Transmission Electron Microscopy (TEM). The morphology, average particle size, and chemical composition of all samples (before and after thermal treatment) were measured using a transmission electron microscopy (TEM) system (Model Tecnai TF 20 X-TWIN, Thermo Fisher Scientific) equipped with a field emission gun, operating at 200 kV. Scanning transmission electron microscopy (SEM) images were taken with the same instrument, using a high-angle annular dark-field detector (STEM-HAADF). For the elemental maps, a Super-X EDS detector was used.

2.2.3. Vibration Sample Magnetometry (VSM). Magnetic properties were probed using a vibrating sample magnetometer (Lake Shore, Model 7407) that was equipped with a variable temperature cryostat (Lake Shore, Model 74018) and a high-temperature oven (Lake Shore, Model 74034). Magnetization versus field loops were collected at 300 K, while temperature dependence profiles were collected upon field cooling at an applied magnetic field of 0.5 T.

2.2.4. Mössbauer Spectroscopy. Mössbauer spectroscopy using ^{57}Fe isotopes was performed in a transmission geometry at 300 K. Measurements were accomplished using a constant-acceleration-type spectrometer (Renon, Model MS-4) with a ^{57}Co radiation source in a Rh matrix kept at room temperature. The 14.4 keV γ-rays were detected with a proportional counter. The absorber surface density was ∼10 mg/cm^2. The spectra were analyzed by means of a least-squares fitting procedure. The isomer shift of the spectrum component is given relative to iron metal at room temperature.

2.2.5. X-ray Absorption Spectroscopy (XAS). XAS at the L-edges of iron and zinc were measured at the PEEM/XAS beamline of the SOLARIS synchrotron. Spectra were collected using total electron yield mode (surface sensitive) at RT and under high vacuum conditions ($p \approx 10^{-9}$ mbar). Dry powders were prepared from nanoparticle solutions sprayed on silicon substrates, left to dry and scanned a few or several times. Energy and intensity drift corrections were obtained for each sample from calibration foil at the beginning of the measurement and additional couple of times, in case the sample was measured for a long time due to, e.g., weak signal. Small changes are caused by indeterminate and seemingly random factors; therefore, for each sample, the mean position of the calibration peak was chosen. Each spectrum is the result of the sum of signals from both the nanoparticles and the substrate. Substrate signal is dependent on coverage with nanoparticles and is generally linear for zinc, strongly nonlinear for Fe L-edge, and presents an additional absorption edge for oxygen from the substrate. For the zinc spectra, background correction consists of the removal of a linear contribution fitted to points before the edge jump. To remove the nonlinear background for iron and oxygen, a clear substrate signal was thoroughly determined and the spectra of samples presenting the strongest signal, presumably with optimal coverage and distinct samples features, were averaged, to obtain the model signal for the Fe/O edge tail for the nanoparticles. Substrate signal was subtracted from the weaker spectra with a factor from 0 to 1, which was chosen to obtain the most similar edge tail, where all the samples have almost the same shape.

XAS spectra at the K-edges of iron and zinc were measured in near edge structure (XANES) and extended fine structure (EXAFS) at the XAFS beamline of ELETTRA (Trieste, Italy). Spectra were collected at RT in transmission mode (volume-sensitive). Energy calibration was accomplished by collecting simultaneously a reference spectrum of metal foil placed in a second experimental chamber after the sample and after the I1 ionization chamber. Nanoparticles in the form of powders were mixed with cellulose matrix using an agate mortar and then compressed into pellets in optimal proportions (thickness resulting in absorption edge-step being close to unity). Each spectrum was collected at least twice, while selected spectra with low edge step at the Zn K-edge, mostly for low zinc concentration, were averaged from up to seven individual scans. Normalization of XANES and extraction of EXAFS signals was performed using Athena software, a part of Demeter X-ray spectroscopy analysis tool pack (v0.9.26).[69] EXAFS signals were extracted using an Hanning window in the k-range 3−12 Å^{-1} for iron and 3−13.5 Å^{-1} for zinc without phase correction, $R_{backgr} = 1$, dk = 0.5, kw = 3, and a spline range in k space from 1.6 Å^{-1}. Numerical calculations of radial distribution functions, $\chi(k)$, of theoretical structures and metal sites were performed using FEFF 10 and converted to radial distributions using an identical set of parameters as the experimental spectra uniformly for every simulated compound.

2.2.6. X-ray Photoelectron Spectroscopy (XPS). XPS tests were performed on samples of nZFN before heating, both in an inert atmosphere and in a vacuum. The spectra were recorded using a PHI 5000 VersaProbe II (ULVAC-PHI, Chigasaki, Japan) spectrometer with a Al Kα monochromatic X-ray beam (E = 1486.6 eV). The spectra were analyzed with particular emphasis on iron and zinc. The elemental composition was calculated based on the determined peak area utilizing software from PHI MultiPak.

3. RESULTS AND DISCUSSION

Thermal stability of the nanoparticles was investigated by means of thermogravimetric and calorimetric measurements. The TG and DSC curves recorded during the decomposition of the ZFN samples (x_{Zn} = 1, 0.86, or 0.35) are shown in Figure 1. In the range up to ∼500 °C, a decrease in mass (TG) was observed in the tested samples (for x_{Zn} = 1 and 0.35), relative to the desorption of previously adsorbed moisture and CO/CO_2.[67] In the case of x_{Zn} = 0.86, this decrease was slightly greater and lasted up to ∼1000 °C. It was related to the decomposition of previously adsorbed organic components during the synthesis process.[35,70]

In the temperature range from ∼500 °C to ∼900−1000 °C, there was practically no decrease in mass (TG, x_{Zn} = 1 and 0.35), and the endothermic peak appearing in this area was associated with the beginning of the process[71,72] of secondary growth of nanoparticles (DSC curve, Figure 1). In the range from ∼1000 °C to 1170 °C, the course of TG curves for all x_{Zn} differed. In the case of x_{Zn} = 1 and 0.86, one stage of weight loss was observed on the TG curve (∼1.25% and 5.76%, respectively; see Figure 1). However, in the case of x_{Zn} = 0.35, two stages of weight loss were observed on the TG curve (the first loss of 1.02% of weight from

https://doi.org/10.1021/acs.iecr.2c01572
Ind. Eng. Chem. Res. 2022, 61, 12532−12544

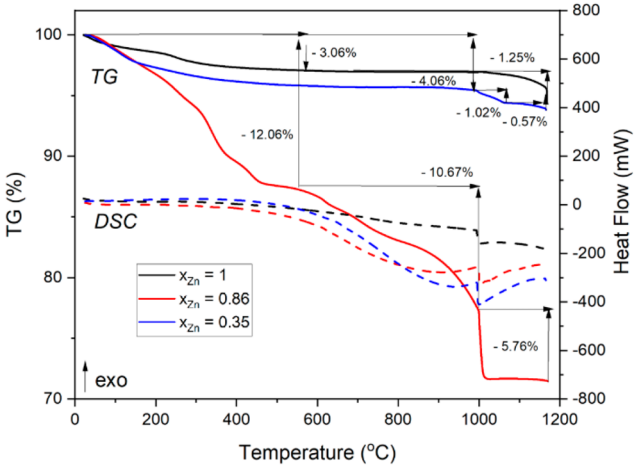

Figure 1. TG/DSC curves of the ZFN with varying degrees of nonstoichiometry (x_{Zn} = 1, 0.86, or 0.35), heated according to the following temperature regime: from 30 °C to 1000 °C at β = 10 °C/min, from 1000 °C to 1170 °C at β = 1 °C/min, and isothermal annealing for 10 min at 1170 °C, in an inert atmosphere.

~1000 °C to 1056 °C, and the second from >1056 °C to 1170 °C (−0.57%), Figure 1). These losses were accompanied by endothermic effects visible on the DSC curve. Morphology of the fresh and vacuum-annealed nanoparticles is shown in Figure 2 for various x_{Zn}. After thermal treatment in a vacuum, sinters are formed which, as suggested by TEM research, consist of nanoparticles of ZnO and iron oxides (see Figures 2 and 3).

Fresh reference sample from Sigma−Aldrich (x_{Zn} = 1) presents much bigger particles than samples obtained from wet synthesis performed for x_{Zn} = 0.86 and 0.35, both with similar sizes. For sample with x_{Zn} = 0.86 treated in vacuum conditions two differing forms can be seen (Figure 3): assemblies with noticeable inner borders (marked as "I") and big, well merged particles ("II"). For the area comprising these two forms, EDS mapping was performed. Figure 3 presents a characteristic map of the elemental distribution of Fe, Zn, and O in the annealed particles. Area I incorporates Zn and O, and area II incorporates Fe and O, which proves that particles after annealing decompose into large, agglomerated Fe_xO_y particles and smaller, weakly bonded ZnO particles. It has previously been reported that hematite (α-Fe_2O_3) appears and disappears during the annealing of zinc ferrite nanoparticles in air or oxygen-rich atmospheres.[73] It was argued that this process is controlled by the oxygen partial pressure. On the other hand, as reported earlier by the authors, under inert conditions, nonisothermal annealing up to 1400 °C of ZFN led to their partial decomposition (~24%). This process included the partial reduction of Fe^{3+} cations to Fe^{2+}, according to the reaction $3Fe_2O_3 \rightarrow 2Fe_3O_4 + {}^1/_2O_2$ and led to the pure crystalline structure of Zn-ferrites with modified stoichiometry.[35]

Field-dependent magnetization measurements performed at RT are shown in Figure 4. They indicate that coercivity of the fresh nanoparticles is negligible in the case of nonstoichiometric ferrites, while a weak hysteresis of ~2 mT is present in the case of the reference sample (x_{Zn} = 1). The shape of magnetization profiles shows also a weak saturation, on the order of 10 Am^2/kg, which is contrary to the purely antiferromagnetic character expected for stoichiometric zinc ferrite. This indicates that the reference sample has a partially inverse spinel structure, leading to a small admixture of magnetic phase, which is a known phenomenon in a case of ZFN.[15,74] Magnetization profile of the x_{Zn} = 0.86 fresh sample show linear dependence, as expected for an antiferromagnet, while that of the x_{Zn} = 0.35 fresh sample shows a tendency to saturate in relatively small fields, which is consistent with the superparamagnetic character of ultrasmall ferrimagnetic nanoparticles of spinel iron oxide doped with zinc,

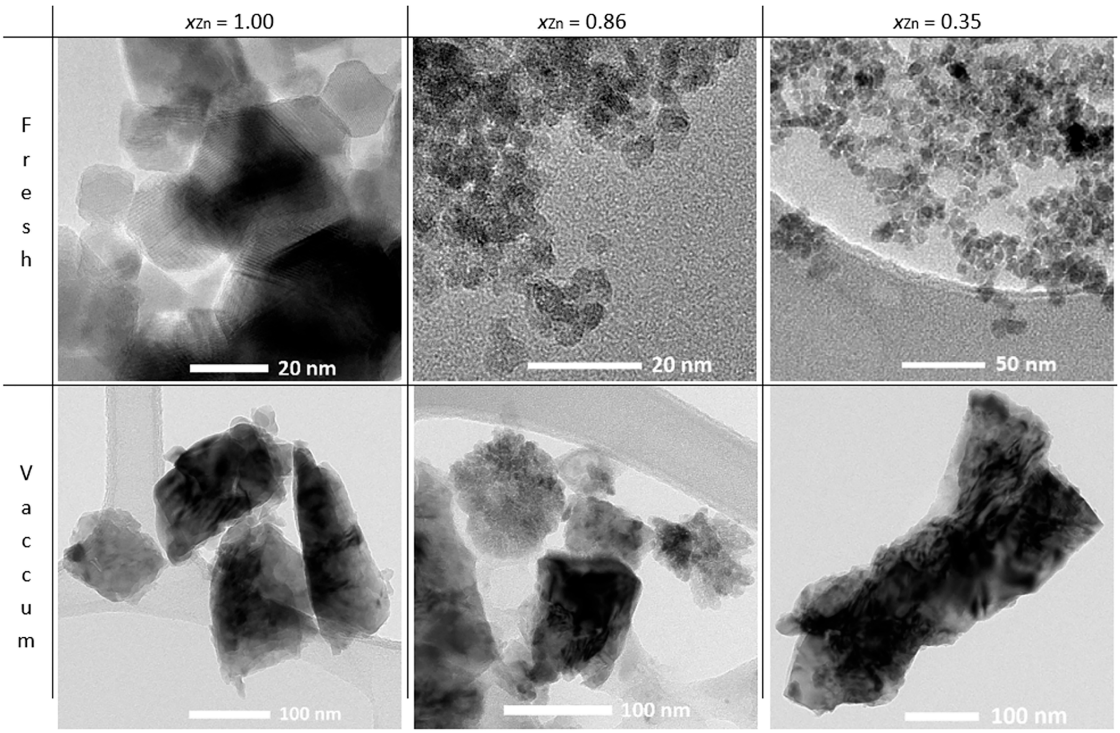

Figure 2. TEM images of fresh and annealed-under-vacuum nanoparticles for x_{Zn} = 1, 0.86, or 0.35.

https://doi.org/10.1021/acs.iecr.2c01572
Ind. Eng. Chem. Res. 2022, 61, 12532−12544

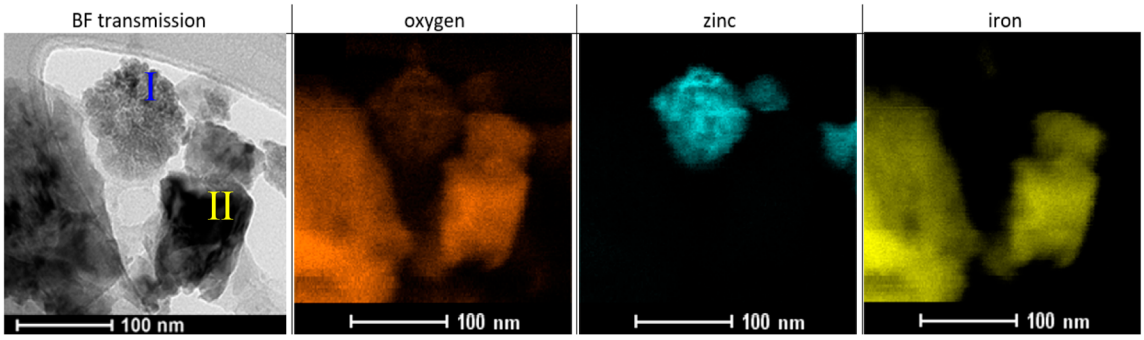

Figure 3. EDS maps comprising two differing forms of particles for sample with x_{Zn} = 0.86 treated under vacuum conditions.

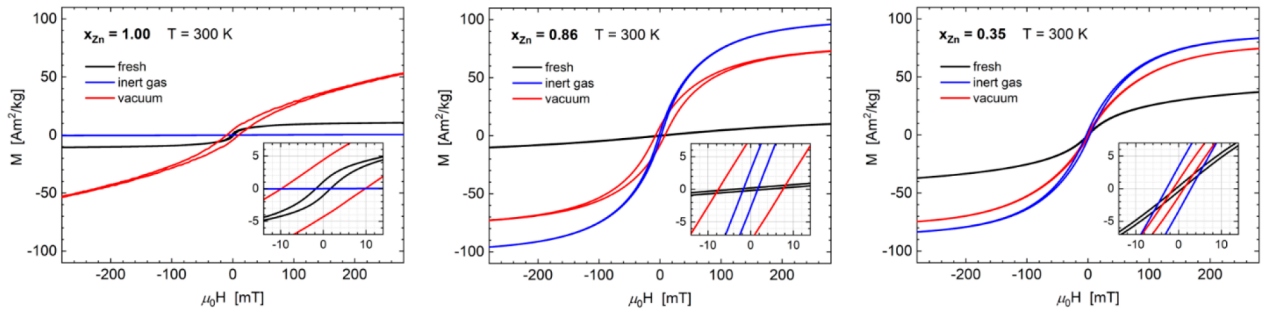

Figure 4. Comparison of magnetic saturation profiles of fresh and annealed samples of nanoparticles with different zinc content. Insets show a closeup of the low magnetic field range, where the evolution of coercivity is easy to perceive.

which is a well-known behavior. In iron oxide nanoparticles with a variable Zn content in the structure, cation distribution has a significantly stronger influence on the magnetic moment of the nanoparticles than the ratio of Zn to Fe, as well as oxygen deficiency. This mechanism is often seen as one of the methods of controlling the magnetic properties of iron oxide nanoparticles.[1,4,8,26,34]

Moreover, it is acknowledged that the magnetic properties of NPs are influenced by the so-called "post-particle surface effects", including a dead layer on the particle surface that consists of many defects, broken chemical bonds, variation of the stoichiometry, arbitrary canting of surface spins, etc.[7] Upon thermal treatment in an inert gas, the magnetic response of a stoichiometric sample (x_{Zn} = 1) decreases to negligible and exhibits linear field dependence, which indicates reconfiguration of ions to perfectly normal spinel. Temperature dependence (Figure 5) shows a decreasing value of magnetization with rising temperature, which is consistent with paramagnetic character with critical temperature significantly below T = 80 K. The other two samples, namely x_{Zn} = 0.86 and 0.35, show a significant increase of RT saturation magnetization up to 70−100 Am^2/kg upon thermal treatment in inert gas.

It indicates that, irrespective of the Zn content of the starting ferrite, the annealing process of nonstoichiometric ferrite leads to phases with different (likely smaller) Zn content and/or predominantly composed of normal spinel, similar to that observed in the x_{Zn} = 1 case.[75] Moreover, the significant opening of hysteresis loop and increase in magnetization slope around zero field indicates increasing magnetic anisotropy. In the case of low Zn content, thermal treatment under vacuum leads to similar magnetic properties as inert gas process, both in terms of coercive field and saturation magnetization. For high Zn content, annealing under vacuum leads to significantly weaker low field magnetization, but higher at high field (see Table 1).

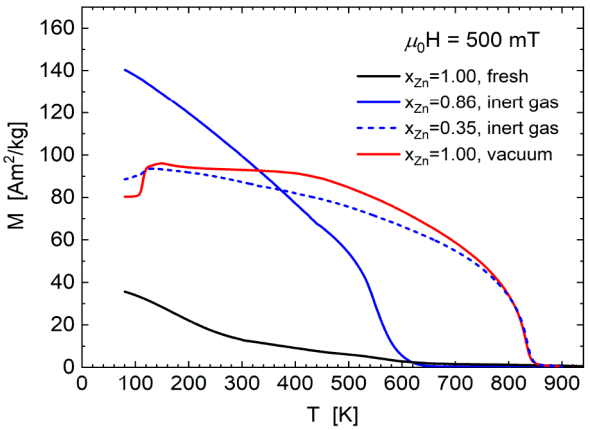

Figure 5. Comparison of selected profiles of temperature-dependent magnetization, which shows multiphase magnetic character of the samples studied and existence of Fe_3O_4 phase (highest T_c and jump at ∼120 K).

These samples reveal much larger coercive fields, ∼8−10 mT, as well as visible high field susceptibility. Such behavior is usually attributed to multiphase character, which seems to fit these samples well. Thermal treatment of ZFN significantly influences the change of their magnetic properties, regardless of the annealing atmosphere and the initial Zn content in the structure. After annealing, all samples except that of $ZnFe_2O_4$ annealed in an inert atmosphere, show a ferromagnetic character with low coercivity, but quite high M_S and $T_C \approx$ 840 K (Figure 5), which proves a significant magnetite content (strong reduction) in the sample structure. The highest increase in M_S, reaching 101 Am^2/kg, was determined for the sample with x_{Zn} = 0.86 annealed in a vacuum. This sample, as the only one among the strongest ferromagnetic samples, does not show the Verwey transition and

https://doi.org/10.1021/acs.iecr.2c01572
Ind. Eng. Chem. Res. 2022, 61, 12532−12544

Table 1. Sample Parameters Determined from VSM Measurements for $Zn_xFe_{3-x}O_4$ before and after Thermal Treatment

sample treatment	T_C[a] [K]	M@1.5T@RT [Am^2/kg]	H_c@RT [mT]
		$x_{Zn} = 1$	
fresh	650	13	2
inert gas	–	0.3	0
vacuum	840	88	10
		$x_{Zn} = 0.86$	
fresh	650	21	4
inert gas	600	101	2
vacuum	840	80	8
		$x_{Zn} = 0.35$	
fresh	750	55	0.5
inert gas	840	86	3
vacuum	840	95	1.5

[a] ±10 K.

its $T_C \approx 600$ K corresponds to the Zn ferrite (Table 1, likely with low Zn content, see spectroscopies). The heating of ZFN under inert conditions probably leads to the formation of one phase which is a solid solution of "initial zinc ferrite" and magnetite Fe_3O_4.[35] In such case, such high values of M_S suggest that, in the newly formed spinel structure, nonmagnetic Zn^{2+} ions occupy Td positions, together with Fe^{3+} ions, according to the formula $(Zn_x^{2+}Fe^{3+}{}_{1-x})[Fe^{2+}{}_{1+x}Fe^{3+}{}_{1-x}]O_4$, where x represents the concentration of Zn ions.[15] However, in the case of vacuum-heated ZFN samples, two forms of particles were observed in the final products (recall Figures 2 and 3), which suggests that these conditions were favoring the formation of multiphase systems such as ZnO and Fe_xO_y, including possibly α-Fe_2O_3 and/or Fe_3O_4, whose presence may significantly affect the magnetic properties (Table 1). α-Fe_2O_3 is antiferromagnetic and therefore can reduce the overall mass magnetization, depending on its share in final products (M_S for α-$Fe_2O_3 = 0.25$ Am^2/kg).[76] Parameters such as M_S, M_R, and H_c are strongly affected by the particle shape, superexchange interactions and anisotropy.[77] As the tests showed, the M_S values for samples annealed under vacuum were slightly higher than that observed under inert conditions (except for the sample $x_{Zn} = 0.86$; see Table 1). This effect can be explained by the presence of the magnetic phase of the Fe_3O_4 type with the simultaneous high crystallinity of the resulting products. The observed differences in the magnetic behavior of the samples suggest that, depending on the atmosphere, final products are formed with a different phase composition (single or multiphase) and with a different degree of crystallinity and amorphization.

In addition, particle shape, superexchange interactions and anisotropy have a strong influence on the magnetic parameters such as M_S, M_R, and H_c, for which the different characters of the ferrite phases are revealed with $M(T)$ dependence. Temperature-magnetization profiles shown in Figure 5 provide an insight into a possible multiphase character of the selected magnetic materials studied (e.g., outlying $x_{Zn} = 0.86$ after inert atmosphere annealing or commercial zinc ferrite). For $x_{Zn} = 1$ magnetic properties are strongly altered by low magnetization of antiferromagnetic ZFN with oxygen impurity, whereas mixed ferrites of different Zn content, upon inert gas annealing, consist of multiphase magnetic iron oxide with large magnetite content. To shed more light on phase composition and its relation to magnetic properties, we have performed a comprehensive set of measurements by means of element-selective spectroscopic probes that involve ^{57}Fe Mössbauer spectroscopy, X-ray photoelectron spectroscopy, and X-ray absorption spectroscopy. They clearly indicate a possible transformation pathway occurring in nanoparticles, especially after annealing in different atmospheres, with particular emphasis on the magnetic phases formed. The ^{57}Fe Mössbauer spectra were recorded at 300 K

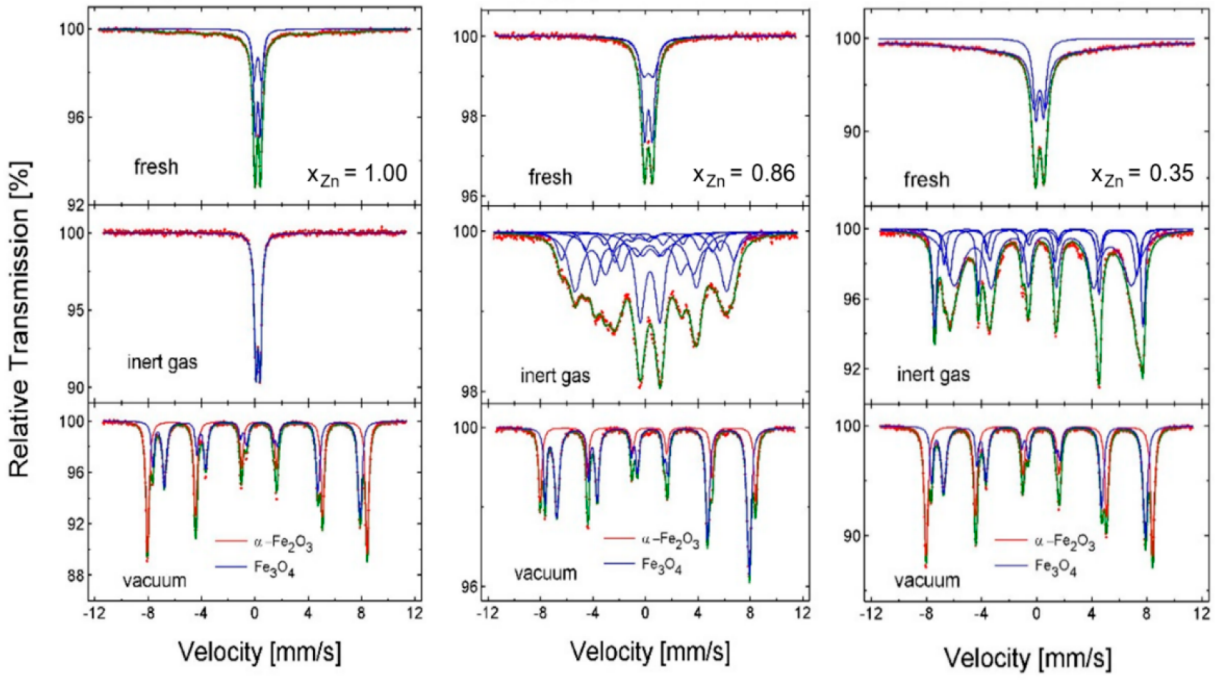

Figure 6. ^{57}Fe Mössbauer spectra recorded at 300 K for $Zn_xFe_{3-x}O_4$ nanoparticles (with $x_{Zn} = 1$, 0.86, or 0.35) and their solid products after annealing at high temperature in an inert atmosphere or under vacuum.

https://doi.org/10.1021/acs.iecr.2c01572
Ind. Eng. Chem. Res. 2022, 61, 12532−12544

Table 2. Phase Composition of the Samples Derived from ^{57}Fe Mössbauer, X-ray Absorption, and X-ray Photoelectron Spectroscopy (Data Collected at 300 K)[a]

sample treatment	component	C_i [%]	⟨IS⟩ [mm/s]	⟨B⟩ [kGs]	⟨QS⟩ [mm/s]	spinel type	Zn Content in volume (K-edge)	Zn Content at surface (L-edge)	Zn/Fe based on XPS data
					x_{Zn} = 1				
fresh	doublet 1	50	0.336	–	0.205	mixed-normal	1.00	1.00	0.75
	doublet 2	50		–	0.237				
inert gas	doublet	100	0.354	–	0.158	normal	0.83	0.58	0.30
vacuum	α-Fe_2O_3	54	0.366	510	−0.061	–	<0.01	0.17	0.12
	Fe_3O_4	46	0.526	462	–				
					x_{Zn} = 0.86				
fresh	doublet 1	51	0.342	–	0.278	mixed-inverse	0.83	0.67	0.52
	doublet 2	49	0.342	–	0.389				
inert gas	doublet set of sextets	18	0.461	–	0.754	normal	0.36	0.54	0.10
		82	0.441	313	–				
vacuum	α-Fe_2O_3	29	0.364	509	−0.063	–	<0.01	<0.01	0.02
	Fe_3O_4	71	0.525	462	–				
					x_{Zn} = 0.35				
fresh	doublet sextet	15	0.338	–	0.277	mixed	0.26	0.24	0.16
		85	0.338	161	–				
inert gas	sextet set of sextets	22	0.267	469	0.003	normal	0.26	0.22	0.04
		78	0.564	408	–				
vacuum	α-Fe_2O_3	52	0.366	510	−0.061	–	<0.01	0.08	0.00
	Fe_3O_4	48	0.527	463	–				

[a]Hyperfine parameters include the type of component, its contribution (C_i), isomer shift (⟨IS⟩), magnetic hyperfine field (⟨B⟩), and quadrupole splitting (⟨QS⟩) values. Dominating spinel type (and possible admixture) as well as chemical composition of particles using volume (~5 μm, K-edge, transmission) and surface (~5 nm, L-edge, electron yield) probing depth were derived from Zn K-edge shape as well as ratio of Zn to Fe K-edge step and ratio of Zn and Fe L-edge step, relative to Zn/Fe, respectively.

(Figure 6) and were analyzed by means of a least-squares fitting procedure with many subspectra components.

Component relative contributions, mean isomer shift ⟨IS⟩ values, mean magnetic hyperfine field ⟨B⟩, and quadrupole splitting ⟨QS⟩ for all samples are presented in Table 2.

As expected, the fresh nonstoichiometric ZFN with x_{Zn} = 0.86 and x_{Zn} = 0.35 are mixed spinels. Based on Mössbauer spectra analysis, the inversion parameter (σ) was estimated to be 0.80 for x_{Zn} = 0.86 and 0.57 for x_{Zn} = 0.35.[35] The atmosphere of thermal treatment play an important role in the formation of solid products. For all x_{Zn} content studied, vacuum annealing leads to decomposition of ferrites. Two distinguished Fe components with high magnetic splitting are present in the spectra with hyperfine interaction parameters characteristic for α-Fe_2O_3 and Fe_3O_4 (Table 2). Their relative contributions are comparable for x_{Zn} = 1 and x_{Zn} = 0.35, but Fe_3O_4 dominates for x_{Zn} = 0.86. Successively, inert atmosphere annealing does not influence iron magnetic interactions for x_{Zn} = 1 but it does for x_{Zn} = 0.86 and 0.35. Several magnetically split subcomponents are needed to fit the spectra. The increase of IS values indicates the possible appearance of Fe^{2+} ions. The resulting solid products are most probably zinc ferrites with a different degree of nonstoichiometry than the fresh ferrite samples.

In view of pronounced magnetic saturation in all the fresh samples studied, the lack of other than doublet components in ^{57}Fe Mössbauer spectra indicates significant relaxation effects. Such effects are characteristic for the smallest superparamagnetic nanoparticles. A single narrow doublet in x_{Zn} = 1.00 sample annealed in an inert atmosphere indicates that the negligible magnetic response is due to the paramagnetic character of this sample, which is attributed to the appearance of an almost stoichiometric normal zinc ferrite phase. The sextet phases observed in the nonstoichiometric samples of x_{Zn} = 0.86 and 0.35 annealed in an inert atmosphere show only weak relaxation, which is consistent with enhanced magnetic response and growth of the mean particle size. The mean hyperfine field of that sample, which is significantly lower than that observed in magnetite and hematite, indicate a significant magnetic inhomogeneity of that sample, which leads to the strong effective magnetic response (magnetic saturation) of these nonstoichiometric ferrites. The sextet components observed in all the samples annealed under vacuum show negligible relaxation effects, consistent with significant growth of the crystallites and increased coercivity.

Note that subsequent annealing cycles under vacuum lead to an increased contribution of the Fe_3O_4 phase, at the cost of the α-Fe_2O_3 phase, up to 100% in the case of x_{Zn} = 1 (see Figure S1 and Table S1 in the Supporting Information). X-ray absorption edges measured for fresh particles with x_{Zn}= 1, 0.86, and 0.35 and after annealing in an inert atmosphere or under vacuum are shown in Figure 7. Radial distribution functions (RDFs) obtained from K-edge EXAFS are shown in Figure 8. Either L- or K-edge for both Fe and Zn show a trend in changes from fresh (untreated) samples, through treated in an inert atmosphere, to annealed under vacuum. Zinc edge spectra are weaker after annealing, with respect to the Fe signal, indicating losses in zinc content in all the samples studied. The loss of Zn is rather small after treatment in an inert atmosphere and significantly larger under vacuum conditions, for which only slight traces of zinc are present. Zn K-edge spectra show a characteristic shape with three distinct peaks in series near the edge, which are characteristic for zinc ferrite. Their respective intensity can be considered as a fingerprint of inverse or normal spinel, since it is strongly dependent on local atomic structure of Zn ions.[78]

https://doi.org/10.1021/acs.iecr.2c01572
Ind. Eng. Chem. Res. 2022, 61, 12532−12544

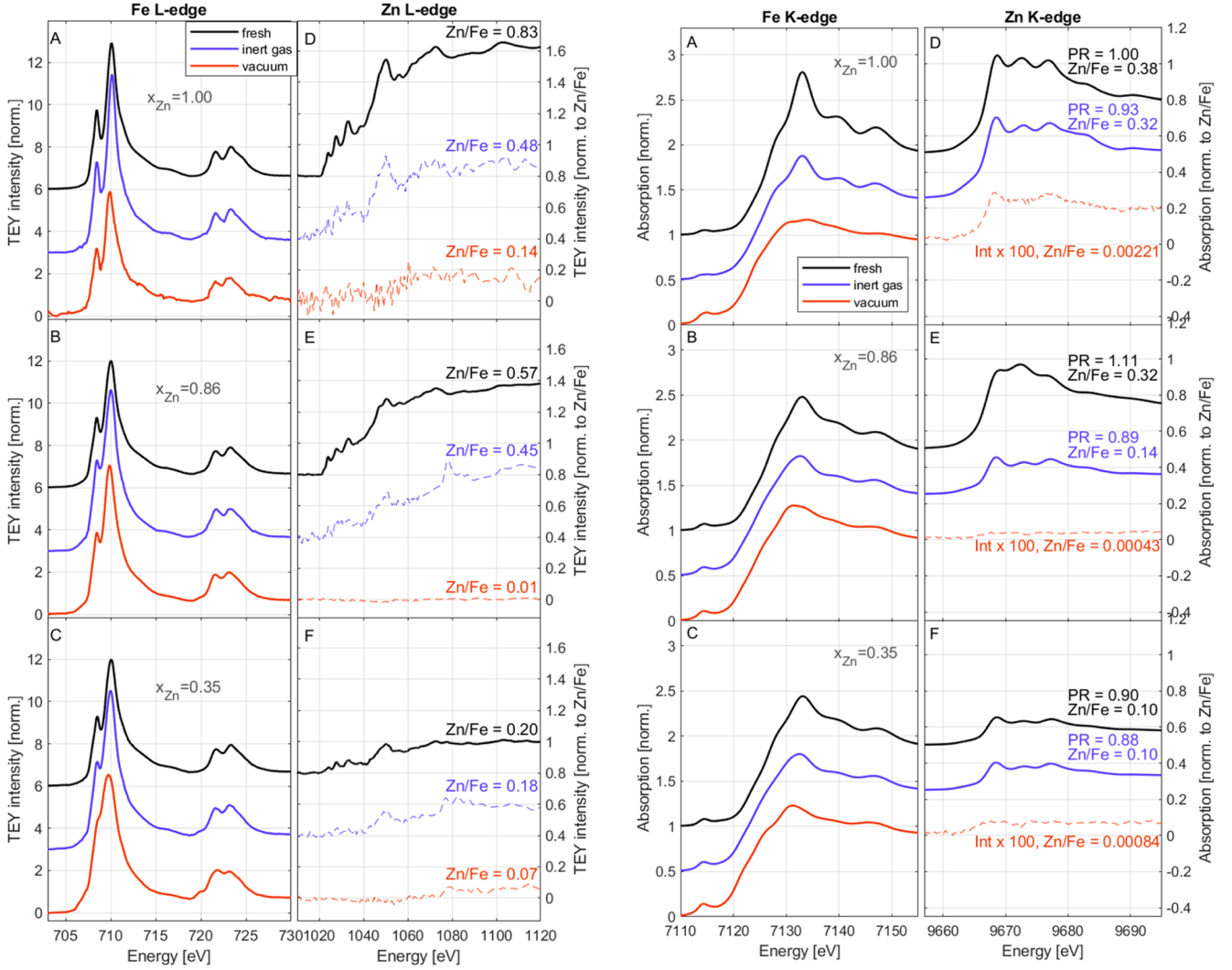

Figure 7. Panels on the left-hand side show the (A−C) Fe and (D−F) Zn L-edge measured by total electron yield and panels on the right-hand side show the (A−C) Fe and (D−F) Zn K-edge measured in transmission, for nZFN with varying degrees of the initial nonstoichiometry (x_{Zn} = 1, 0.86, or 0.35), after no treatment, and after annealing in an inert atmosphere or under vacuum. All edges are normalized with respect to edge jump at the Fe edges. The ratio of edge jump between Zn and Fe spectra, i.e., Ze/Fe, is denoted for each sample for both techniques. Dashed plot lines indicate approaching the detection limit or very weak signal, with respect to background. "PR" for the Zn K-edge is the ratio of the middle peak just after Zn K-edge to mean intensity of its neighbors, which indicates higher inversion of the spinel structure for lower PR. Although very good sensitivity for the Zn K-edge is visible, it is not possible to discern post-edge peaks after annealing under vacuum.

Evolution of these spectra shows, in most cases, a clear transformation from mixed to normal structure after annealing (Table 2). Regarding Fe L_3- or L_2-edge spectra, the dip between the main peaks is vanishing, leading to a spectral shape similar to that of magnetic iron oxides: maghemite (weak dips) or magnetite (no dip at the L_3-edge). Fe K-edge features become less distinct, apart from rising pre-edge peak intensity and signal between the prepeak and the edge, suggesting a progressive amorphization. Position of Fe K-edge moves toward lower energies, indicating a reduction of Fe ions, which is stronger for vacuum-annealed samples. The shift is ∼1 eV for annealing in an inert atmosphere and 2 eV for vacuum-annealed samples.

Such shift is attributed to the decreasing amount of Zn (lower effective x_{Zn}) and formation of Fe_3O_4 phase. RDF information from Fe K-edge EXAFS spectra (Figures 8A−C) show a tendency to decrease in peak intensity at ∼5.5 Å and an increase in the intensity of the peak at ∼3.1 Å. Such behavior implies a change of iron site occupancy from Oh to Td (compare with ∼2.8 Å for x_{Zn} = 0.86 and 0.35 after annealing under vacuum), suggesting the appearance of the hematite phase for these samples and conditions.

Overall, vacuum conditions seem to result in slight amorphization of samples, whereas heating in an inert atmosphere has a tendency to improve crystallization. The RDF for Zn ions (Figure 8E−G) clearly exposes the fact that Zn has almost the same, highly crystallized surroundings for every x_{Zn} after annealing in an inert atmosphere. The peak emerging at ∼6.3 Å and no dips at ∼5 Å suggests the presence of the ZnO phase. Generally, for both Fe and Zn spectra of the annealed samples, next-neighbors coordination spheres are much more pronounced, compared to fresh samples. This is a clear indication of increased size of crystallites. Transformation to pure magnetite is evident only from the L-edge of the low Zn content (x_{Zn} = 0.35) sample, but there is a clear dependence of dip magnitude in the L_3- or L_2-edge double peak on x_{Zn}: it decreases as the content decreases, signifying magnetism for

https://doi.org/10.1021/acs.iecr.2c01572
Ind. Eng. Chem. Res. 2022, 61, 12532−12544

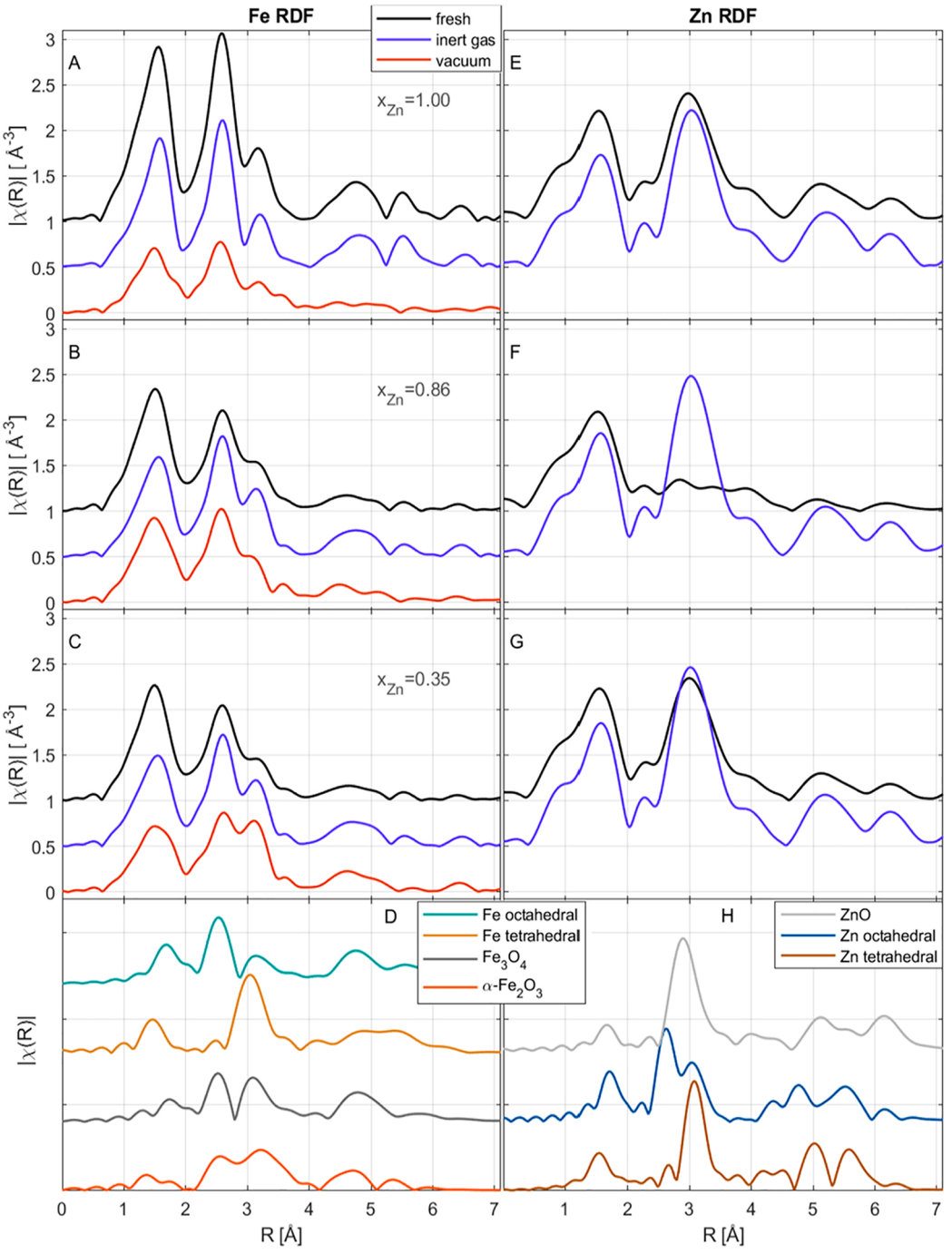

Figure 8. Radial distribution information obtained from EXAFS for (A−C, left) iron and (E−G, right) zinc for varying x_{Zn} and treatment. The lowest row presents numerically calculated RDF for related compounds for iron (panel (D)) and zinc (panel (H)) in the ferrite spinel structure for the positions of both the tetrahedral and octahedral ions.

lower x_{Zn}. Apart from clear, distinct features of fresh stoichiometric zinc ferrite, the Zn K-edge does not provide much information, with regard to the influence of zinc content on structural changes in the nanoparticles studied. However, from Fe RDF data (Figure 8A−C) it seems that, for lower x_{Zn}, there are less Fe ions in Oh sites and thus, possibly, more Zn ions, which results in a spinel structure closer to inverse, and for higher x_{Zn}, a structure closer to normal. Unfortunately, EXAFS for Zn ions cannot support this inference, since Zn has almost the same surroundings for every x_{Zn}, also suggesting the ZnO phase rather than $ZnFe_2O_4$ phase. The Zn/Fe edge step ratio is evolving notably stronger at the K-edge, which is measured in transmission and is sensitive to volume composition of the sample. It clearly shows that all of the samples annealed under vacuum have a negligible amount of Zn in its volume. (Please see Table 2 for the expected stoichiometry parameter as derived from K-edge spectra using XAFSmass software.[79]) In the case of the L-edge, which are sensitive to couple of nanometers,[80] the evolution of edge step shows some fraction of Zn at the surface also in vacuum-annealed samples and a significantly smaller density of Zn, with respect to Fe, in the near surface regions (cf. Table 2). Based on comparison of these results, it is remarkable

https://doi.org/10.1021/acs.iecr.2c01572
Ind. Eng. Chem. Res. 2022, 61, 12532−12544

that all samples annealed in an inert atmosphere show passivation and Zn deficiency in the surface. To further support qualitative conclusions based on the analysis of L-edge XAS data regarding surface chemistry of the samples studied, we have performed XPS measurement for particles with x_{Zn} = 1, 0.86, and 0.35, fresh and after annealing in an inert atmosphere or under vacuum. Results of quantitative analysis of these spectra are shown in Table S2 in the Supporting Information and Table 3.

Table 3. Quantitative Analysis of the Fe Ionic Distribution in the Near-Surface Phases Based on the Fitting of Peaks with Characteristic Energy in the Fe $2p_{3/2}$ XPS Spectrum

	Area (%)		
treatment	Fe^{2+}_{Oh}: BE = 709.2 eV	Fe^{3+}_{Oh}: BE = 710.5 eV	Fe^{3+}_{Td}: BE = 712.0 eV
Fresh			
x_{Zn} = 1	12.00	19.57	68.43
x_{Zn} = 0.86	11.17	40.45	48.38
x_{Zn} = 0.35	21.70	34.19	44.12
Inert Gas Atmosphere			
x_{Zn} = 1	20.86	45.90	33.24
x_{Zn} = 0.86	22.07	47.39	30.54
x_{Zn} = 0.35	27.40	49.05	23.55
Under Vacuum			
x_{Zn} = 1	15.38	50.33	31.29
x_{Zn} = 0.86	29.44	44.33	26.22
x_{Zn} = 0.35	31.23	40.51	28.25

The XPS measurements performed on fresh nonstoichiometric zinc ferrites (fresh) confirmed the presence of both Zn and Fe in the structure. The determined Zn/Fe ratio for the fresh nZFN increased linearly (cf. Table S2).

On the other hand, after heating, regardless of the type of atmosphere (inert or vacuum), in all analyzed solid products, there is a clear decrease in the Zn content in the structure, which suggests its sublimation.[35] The XPS spectrum of $Fe^2p_{3/2}$ analysis showed that, in the case of nZFN samples annealed in an inert atmosphere, the content of Fe^{2+} ions increased (by a factor of ~2), compared to fresh nZFN. However, for nZFN samples annealed in a vacuum atmosphere (Table 3), the degree of reduction was almost three times higher. This is probably due to the fact that, under vacuum conditions, one of the gaseous reaction products (O_2) is removed from the reaction medium, which causes the reaction equilibrium to shift toward the reduction.

Regardless of the type of atmosphere, there is a tendency for easier reduction of Fe^{3+} ions and diffusion from tetrahedral sites.

4. CONCLUSIONS

Thermal treatment has a significant impact on the microstructure, phase composition, and cation distribution in spinel ferrites, which, in turn, affects their magnetic properties. In this study, we show how the annealing of the nZFN leads to materials with different magnetic and structural properties that are dependent on the type of annealing atmosphere. The subject of the research were nZFN produced by the wet chemistry method.[35] Effects of two types of atmosphere (inert and vacuum) are identified.

Annealing, irrespective of the type of atmosphere, led to a partial reduction of Fe^{3+} ions to Fe^{2+} and an increase in the size of the particles. The heat treatment of ZFN in an inert atmosphere favors the crystallization, while vacuum annealing favors also the amorphization of the sample surfaces (see Figures 7 and 8). The main magnetic parameters show a severe variation, as a result of heat-treated nZFN (e.g., x_{Zn} = 0.86), depending on the atmosphere: the saturation magnetization (M_S) increase from 21 to 101 emu/g or 80, the coercive field (H_c) decreases from 4 to 2 mT or increases to 8 mT, respectively, for an inert atmosphere or under vacuum. The type of atmosphere strongly influences the final products formed (monophasic spinel ferrites with different stoichiometry or multiphase systems), as well as their magnetic properties. The research suggests that the use of an inert atmosphere promotes the formation of one phase systems, where the solid end product is zinc ferrite (ZF), which is a solid solution of magnetite and zinc ferrite with a reduced Zn content in the structure. Because of high temperature in the inert atmosphere, "new ferrites" are formed as a result of partial reduction of Fe^{3+} ions to Fe^{2+} and ZnO sublimation.[35] In an inert atmosphere, cation redistribution occurs, ordering the spinel toward the normal spinel structure, with Zn ions moving to the tetrahedral sites. For nZFN samples, apart from the normal spinel phase preference, a decrease in Zn content was also observed. Both of these effects lead to an enhancement of the magnetic response up to M_S values of 101 Am^2/kg. This effect is also confirmed by changes in the position of oxygen in the spinel structure. On the other hand, heating under vacuum conditions with high probability promotes the formation of multiphase systems in which ZnO, Fe_3O_4, and/or Fe_2O_3 occurs (see Figures 3 and 6).This is suggested by the results of XAS and Mössbauer spectroscopies and TEM imaging. Relative content of Fe_2O_3 and Fe_3O_4 in the final products increases as the number of annealing cycles increases. This is a confirmation that the final solid product with complete decomposition of ZFN is magnetite. In the considered conditions, thermal decomposition of nZFN in a vacuum probably leads to the formation of magnetic oxides that exhibit high M_S values, thus changes in the magnetization are most probably introduced mainly by these emerging oxides. Results shown in this document describe how a thermal treatment of spinel ferrite nanoparticles can be used as a "handle" to adjust the structure and cation distribution in nanoparticles and, therefore, create materials with enhanced magnetic properties and can be used to foresee material behavior under harsh conditions. It seems that the physical properties of the end products after both vacuum and inert atmosphere annealing can be controlled to be useful in technical applications such as modified magnetic materials, high-temperature sorbents, or in the production of O_2 and/or H_2 using solar energy.[48−50,52−54,57,58]

■ ASSOCIATED CONTENT

Supporting Information

The Supporting Information is available free of charge at https://pubs.acs.org/doi/10.1021/acs.iecr.2c01572.

^{57}Fe Mössbauer spectra recorded at 300 K for $Zn_xFe_{3-x}O_4$ NPs annealed in vacuum once and twice for x_{Zn} = 1 and 0.35 (Figure S1); ^{57}Fe Mössbauer spectral parameters for above-mentioned spectra (Table S1); Amount of elements based on analysis of atomic concentration (XPS data) for samples before and after thermal treatment (Table S2) (PDF)

https://doi.org/10.1021/acs.iecr.2c01572
Ind. Eng. Chem. Res. 2022, 61, 12532−12544

AUTHOR INFORMATION

Corresponding Authors

Juliusz Kuciakowski − *AGH University of Science and Technology, Academic Centre for Materials and Nanotechnology, 30-059 Krakow, Poland; AGH University of Science and Technology, Faculty of Physics and Applied Computer Science, 30-059 Krakow, Poland*; Email: jkuciako@agh.edu.pl

Marcin Sikora − *AGH University of Science and Technology, Academic Centre for Materials and Nanotechnology, 30-059 Krakow, Poland*; Email: marcin.sikora@agh.edu.pl

Angelika Kmita − *AGH University of Science and Technology, Academic Centre for Materials and Nanotechnology, 30-059 Krakow, Poland*; orcid.org/0000-0001-8634-2084; Email: akmita@agh.edu.pl

Authors

Joanna Stępień − *AGH University of Science and Technology, Academic Centre for Materials and Nanotechnology, 30-059 Krakow, Poland*

Jan Żukrowski − *AGH University of Science and Technology, Academic Centre for Materials and Nanotechnology, 30-059 Krakow, Poland*

Dorota Lachowicz − *AGH University of Science and Technology, Academic Centre for Materials and Nanotechnology, 30-059 Krakow, Poland*; orcid.org/0000-0001-9394-5297

Antoni Żywczak − *AGH University of Science and Technology, Academic Centre for Materials and Nanotechnology, 30-059 Krakow, Poland*; orcid.org/0000-0001-9554-3742

Marta Gajewska − *AGH University of Science and Technology, Academic Centre for Materials and Nanotechnology, 30-059 Krakow, Poland*

Marek Przybylski − *AGH University of Science and Technology, Academic Centre for Materials and Nanotechnology, 30-059 Krakow, Poland; AGH University of Science and Technology, Faculty of Physics and Applied Computer Science, 30-059 Krakow, Poland*; orcid.org/0000-0002-6479-7886

Simone Pollastri − *Elettra - Sincrotrone Trieste S.C.p.A, 34149 Basovizza, Trieste, Italy*; orcid.org/0000-0001-5332-260X

Luca Olivi − *Elettra - Sincrotrone Trieste S.C.p.A, 34149 Basovizza, Trieste, Italy*

Complete contact information is available at: https://pubs.acs.org/10.1021/acs.iecr.2c01572

Author Contributions

The manuscript was written through contributions of all authors. All authors have given approval to the final version of the manuscript.

Funding

This work was supported by the National Science Centre, Poland, grant number 2016/23/D/ST8/00013.-The authors acknowledge the CERIC-ERIC Consortium for the access to experimental facilities.

Notes

The authors declare no competing financial interest.

REFERENCES

(1) Yang, Y.; Liu, X.; Yang, Y.; Xiao, W.; Li, Z.; Xue, D.; Li, F.; Ding, J. Synthesis of Nonstoichiometric Zinc Ferrite Nanoparticles with Extraordinary Room Temperature Magnetism and Their Diverse Applications. *J. Mater. Chem. C* **2013**, *1* (16), 2875−2885.

(2) Lachowicz, D.; Wirecka, R.; Górka-Kumik, W.; Marzec, M. M.; Gajewska, M.; Kmita, A.; Żukrowski, J.; Sikora, M.; Zapotoczny, S.; Bernasik, A. Gradient of Zinc Content in Core-Shell Zinc Ferrite Nanoparticles-Precise Study on Composition and Magnetic Properties. *Phys. Chem. Chem. Phys.* **2019**, *21* (42), 23473−23484.

(3) Kowalik, P.; Bujak, P.; Penkala, M.; Kotwica, K.; Kmita, A.; Gajewska, M.; Ostrowski, A.; Pron, A. Synthesis of $CuFeS_{2-x}Se_x$-Alloyed Nanocrystals with Localized Surface Plasmon Resonance in the Visible Spectral Range. *J. Mater. Chem. C* **2019**, *7* (21), 6246−6250.

(4) Kmita, A.; Lachowicz, D.; Zukrowski, J.; Gajewska, M.; Szczerba, W.; Kuciakowski, J.; Zapotoczny, S.; Sikora, M. One-Step Synthesis of Long Term Stable Superparamagnetic Colloid of Zinc Ferrite Nanorods in Water. *Materials (Basel)* **2019**, *12* (7), 1048.

(5) Unni, M.; Uhl, A. M.; Savliwala, S.; Savitzky, B. H.; Dhavalikar, R.; Garraud, N.; Arnold, D. P.; Kourkoutis, L. F.; Andrew, J. S.; Rinaldi, C. Thermal Decomposition Synthesis of Iron Oxide Nanoparticles with Diminished Magnetic Dead Layer by Controlled Addition of Oxygen. *ACS Nano* **2017**, *11* (2), 2284−2303.

(6) Qin, M.; Shuai, Q.; Wu, G.; Zheng, B.; Wang, Z.; Wu, H. Zinc Ferrite Composite Material with Controllable Morphology and Its Applications. *Mater. Sci. Eng. B: Solid-State Mater. Adv. Technol.* **2017**, *224* (May), 125−138.

(7) Szczerba, W.; Zukrowski, J.; Przybylski, M.; Sikora, M.; Safonova, O.; Shmeliov, A.; Nicolosi, V.; Schneider, M.; Granath, T.; Oppmann, M.; Straßer, M.; Mandel, K. Pushing up the Magnetisation Values for Iron Oxide Nanoparticles: Via Zinc Doping: X-Ray Studies on the Particle's Sub-Nano Structure of Different Synthesis Routes. *Phys. Chem. Chem. Phys.* **2016**, *18* (36), 25221−25229.

(8) Lachowicz, D.; Górka, W.; Kmita, A.; Bernasik, A.; Zukrowski, J.; Szczerba, W.; Sikora, M.; Kapusta, C.; Zapotoczny, S. Enhanced Hyperthermic Properties of Biocompatible Zinc Ferrite Nanoparticles with a Charged Polysaccharide Coating. *J. Mater. Chem. B* **2019**, *7* (18), 2962−2973.

(9) Kuciakowski, J.; Kmita, A.; Lachowicz, D.; Wytrwal-Sarna, M.; Pitala, K.; Lafuerza, S.; Koziej, D.; Juhin, A.; Sikora, M. Selective Magnetometry of Superparamagnetic Iron Oxide Nanoparticles in Liquids. *Nanoscale* **2020**, *12* (31), 16420−16426.

(10) Bujak, P.; Wróbel, Z.; Penkala, M.; Kotwica, K.; Kmita, A.; Gajewska, M.; Ostrowski, A.; Kowalik, P.; Pron, A. Highly Luminescent Ag-In-Zn-S Quaternary Nanocrystals: Growth Mechanism and Surface Chemistry Elucidation. *Inorg. Chem.* **2019**, *58* (2), 1358−1370.

(11) Kowalik, P.; Penkala, M.; Bujak, P.; Kmita, A.; Gajewska, M.; Ostrowski, A.; Slodek, A.; Pron, A. From Ag_2S to Luminescent Ag-In-S Nanocrystals: Via an Ultrasonic Method-an in Situ Synthesis Study in an NMR Tube. *J. Mater. Chem. C* **2020**, *8* (26), 8942−8952.

(12) Hufnagel, A. G.; Peters, K.; Müller, A.; Scheu, C.; Fattakhova-Rohlfing, D.; Bein, T. Photoelectrochemistry: Zinc Ferrite Photoanode Nanomorphologies with Favorable Kinetics for Water-Splitting. *Adv. Funct. Mater.* **2016**, *26* (25), 4425.

(13) Bañobre-López, M.; Bran, C.; Rodríguez-Abreu, C.; Gallo, J.; Vázquez, M.; Rivas, J. A. Colloidally Stable Water Dispersion of Ni Nanowires as an Efficient: T2-MRI Contrast Agent. *J. Mater. Chem. B* **2017**, *5* (18), 3338−3347.

(14) Cador, O.; Grasset, F.; Haneda, H.; Etourneau, J. Memory Effect And Super-Spin-Glass Ordering In An Aggregated Nanoparticle Sample. *J. Magn. Magn. Mater.* **2004**, *268* (1−2), 232−236.

(15) Grasset, F.; Labhsetwar, N.; Li, D.; Park, D. C.; Saito, N.; Haneda, H.; Cador, O.; Roisnel, T.; Mornet, S.; Duguet, E.; Portier, J.; Etourneau, J. Synthesis and Magnetic Characterization of Zinc Ferrite Nanoparticles with Different Environments: Powder, Colloidal Solution, and Zinc Ferrite−Silica Core−Shell Nanoparticles. *Langmuir* **2002**, *18* (21), 8209−8216.

(16) Bajorek, A.; Berger, C.; Dulski, M.; Łopadczak, P.; Zubko, M.; Prusik, K.; Wojtyniak, M.; Chrobak, A.; Grasset, G.; Randrianantoandro, N. Microstructural and Magnetic Characterization of $Ni_{0.5}Zn_{0.5}Fe_2O_4$ Ferrite Nanoparticles. *J. Phys. Chem. Solids* **2019**, *129*, 1−21.

(17) Bram, S.; Gordon, M. N.; Carbonell, M. A.; Pink, M.; Stein, B. D.; Morgan, D. G.; Aguilà, D.; Aromí, G.; Skrabalak, S. E.; Losovyj, Y.; Bronstein, L. M. Zn^{2+} Ion Surface Enrichment in Doped Iron Oxide Nanoparticles Leads to Charge Carrier Density Enhancement. *ACS Omega* **2018**, *3* (11), 16328−16337.
(18) Kmita, A.; Pribulova, A.; Holtzer, M.; Futas, P.; Roczniak, A. Use of Specific Properties of Zinc Ferrite in Innovative Technologies. *Arch. Metall. Mater.* **2016**, *61* (4), 2141−2146.
(19) Jia, Z.; Ren, D.; Liang, Y.; Zhu, R. A New Strategy for the Preparation of Porous Zinc Ferrite Nanorods with Subsequently Light-Driven Photocatalytic Activity. *Mater. Lett.* **2011**, *65* (19−20), 3116−3119.
(20) Fan, G.; Gu, Z.; Yang, L.; Li, F. Nanocrystalline Zinc Ferrite Photocatalysts Formed Using the Colloid Mill and Hydrothermal Technique. *Chem. Eng. J.* **2009**, *155* (1−2), 534−541.
(21) Kmita, A.; Żukrowski, J.; Hodor, K.; Smogór, H.; Sikora, M. Zinc Ferrite Nanoparticles as Perspective Functional Materials for Applications in Casting Technologies. *Metalurgija* **2017**, *56* (1−2), 29−32.
(22) Pawlaczyk, M.; Schroeder, G. *Hybrydowe Nanomateriały Magnetyczne*; Wydanie, I., Ed.; Cursiva: Kostrzyn, Poland, 2017.
(23) Nemati, Z.; Alonso, J.; Rodrigo, I.; Das, R.; Garaio, E.; García, J. Á.; Orue, I.; Phan, M. H.; Srikanth, H. Improving the Heating Efficiency of Iron Oxide Nanoparticles by Tuning Their Shape and Size. *J. Phys. Chem. C* **2018**, *122* (4), 2367−2381.
(24) Revia, R. A.; Zhang, M. Magnetite Nanoparticles for Cancer Diagnosis, Treatment, and Treatment Monitoring: Recent Advances. *Mater. Today* **2016**, *19*, 157−168.
(25) Gavilán, H.; Kowalski, A.; Heinke, D.; Sugunan, A.; Sommertune, J.; Varón, M.; Bogart, L. K.; Posth, O.; Zeng, L.; González-Alonso, D.; et al. Colloidal Flower-Shaped Iron Oxide Nanoparticles: Synthesis Strategies and Coatings. *Part. Part. Syst. Charact.* **2017**, *34* (7), 1−12.
(26) Kharisov, B. I.; Dias, H. V. R.; Kharissova, O. V. Mini-Review: Ferrite Nanoparticles in the Catalysis. *Arab. J. Chem.* **2019**, *12* (7), 1234−1246.
(27) Giustini, A. J.; Petryk, A. A.; Cassim, S. M.; Tate, J. A.; Baker, I.; Hoopes, P. J. Magnetic Nanoparticle Hyperthermia in Cancer Treatment. *Nano Life* **2010**, *01* (01n02), 17−32.
(28) Sanchez-Lievanos, K. R.; Stair, J. L.; Knowles, K. E. Cation Distribution in Spinel Ferrite Nanocrystals: Characterization, Impact on Their Physical Properties, and Opportunities for Synthetic Control. *Inorg. Chem.* **2021**, *60* (7), 4291−4305.
(29) Hanini, A.; Lartigue, L.; Gavard, J.; Kacem, K.; Wilhelm, C.; Gazeau, F.; Chau, F.; Ammar, S. Zinc Substituted Ferrite Nanoparticles with $Zn_{0.9}Fe_{2.1}O_4$ Formula Used as Heating Agents for in Vitro Hyperthermia Assay on Glioma Cells. *J. Magn. Magn. Mater.* **2016**, *416*, 315−320.
(30) Lohr, J.; De Almeida, A. A.; Moreno, M. S.; Troiani, H.; Goya, G. F.; Torres Molina, T. E.; Fernandez-Pacheco, R.; Winkler, E. L.; Vasquez Mansilla, M.; Cohen, R.; Nagamine, L. C. C. M.; Rodríguez, L. M.; Fregenal, D. E.; Zysler, R. D.; Lima, E. Effects of Zn Substitution in the Magnetic and Morphological Properties of Fe-Oxide-Based Core-Shell Nanoparticles Produced in a Single Chemical Synthesis. *J. Phys. Chem. C* **2019**, *123* (2), 1444−1453.
(31) Goya, G. F.; Rechenberg, H. R. Ionic Disorder and Néel Temperature in $ZnFe_2O_4$ Nanoparticles. *J. Magn. Magn. Mater.* **1999**, *196−197*, 191−192.
(32) Akhtar, M. J.; Nadeem, M.; Javaid, S.; Atif, M. Cation Distribution in Nanocrystalline $ZnFe_2O_4$ Investigated Using X-Ray Absorption Fine Structure Spectroscopy. *J. Phys.: Condens. Matter* **2009**, *21* (40), 405303.
(33) Hölscher, J.; Andersen, H. L.; Saura-Múzquiz, M.; Garbus, P. G.; Christensen, M. Correlation between Microstructure, Cation Distribution and Magnetism in $Ni_{1-X}Zn_xFe_2O_4$ Nanocrystallites. *CrystEngComm* **2020**, *22* (3), 515−524.
(34) Kavas, H.; Baykal, A.; Toprak, M. S.; Köseoğlu, Y.; Sertkol, M.; Aktaş, B. Cation Distribution and Magnetic Properties of Zn Doped $NiFe_2O_4$ Nanoparticles Synthesized by PEG-Assisted Hydrothermal Route. *J. Alloys Compd.* **2009**, *479* (1−2), 49−55.
(35) Kmita, A.; Żukrowski, J.; Kuciakowski, J.; Marciszko-Wiąckowska, M.; Żywczak, A.; Lachowicz, D.; Gajewska, M.; Sikora, M. Effect of Thermal Treatment at Inert Atmosphere on Structural and Magnetic Properties of Non-Stoichiometric Zinc Ferrite Nanoparticles. *Metall. Mater. Trans. A Phys. Metall. Mater. Sci.* **2021**, *52* (5), 1632−1648.
(36) Vucinic-Vasic, M.; Bozin, E. S.; Bessais, L.; Stojanovic, G.; Kozmidis-Luburic, U.; Abeykoon, M.; Jancar, B.; Meden, A.; Kremenovic, A.; Antic, B. Thermal Evolution of Cation Distribution/Crystallite Size and Their Correlation with the Magnetic State of Yb-Substituted Zinc Ferrite Nanoparticles. *J. Phys. Chem. C* **2013**, *117* (23), 12358−12365.
(37) Bræstrup, F.; Hauback, B. C.; Hansen, K. K. Temperature Dependence of the Cation Distribution in $ZnFe_2O_4$ Measured with High Temperature Neutron Diffraction. *J. Solid State Chem.* **2008**, *181* (9), 2364−2369.
(38) Kamiyama, T.; Haneda, K.; Sato, T.; Ikeda, S.; Asano, H. Cation Distribution in $ZnFe_2O_4$ Fine Particles Studied by Neutron Powder Diffraction. *Solid State Commun.* **1992**, *81* (7), 563−566.
(39) Shin, T. H.; Choi, Y.; Kim, S.; Cheon, J. Recent Advances in Magnetic Nanoparticle-Based Multi-Modal Imaging. *Chem. Soc. Rev.* **2015**, *44*, 4501−4516.
(40) Philip, J.; Laskar, J. M. Optical Properties and Applications of Ferrofluids - A Review. *J. Nanofluids* **2012**, *1* (1), 3−20.
(41) Wu, C.; Xu, Y.; Xu, S.; Tu, J.; Tian, C.; Lin, Z. Enhanced Adsorption of Arsenate by Spinel Zinc Ferrite Nano Particles: Effect of Zinc Content and Site Occupation. *J. Environ. Sci. (China)* **2019**, *79*, 248−255.
(42) Pham, T. N.; Huy, T. Q.; Le, A. T. Spinel Ferrite (AFe_2O_4)-Based Heterostructured Designs for Lithium-Ion Battery, Environmental Monitoring, and Biomedical Applications. *RSC Adv.* **2020**, *10* (52), 31622−31661.
(43) Singh, A.; Singh, A.; Singh, S.; Tandon, P.; Yadav, B. C.; Yadav, R. R. Synthesis, Characterization and Performance of Zinc Ferrite Nanorods for Room Temperature Sensing Applications. *J. Alloys Compd.* **2015**, *618*, 475−483.
(44) Seifi, H.; Gholami, T.; Seifi, S.; Ghoreishi, S. M.; Salavati-Niasari, M. A Review on Current Trends in Thermal Analysis and Hyphenated Techniques in the Investigation of Physical, Mechanical and Chemical Properties of Nanomaterials. *J. Anal. Appl. Pyrolysis* **2020**, *149*, 104840.
(45) Mansfield, E. Recent Advances in Thermal Analysis of Nanoparticles: Methods, Models and Kinetics. In *Modeling, Characterization and Production of Nanomaterials: Electronics, Photonics and Energy Applications*; Elsevier, 2015; pp 167−178, DOI: 10.1016/B978-1-78242-228-0.00006-5.
(46) Walter, D.; Buxbaum, G.; Laqua, W. The Mechanism of the Thermal Transformation from Goethite to Hematite. *J. Therm. Anal. Calorim.* **2001**, *63* (3), 733−748.
(47) Kalska-Szostko, B.; Wykowska, U.; Satula, D.; Nordblad, P. Thermal Treatment of Magnetite Nanoparticles. *Beilstein J. Nanotechnol.* **2015**, *6* (1), 1385−1396.
(48) Yaghmour, S. J.; Hafez, M.; Ali, K.; Elshirbeeny, W. The Influence of Zinc Ferrites Nanoparticles on the Thermal, Mechanical, and Magnetic Properties of Rubber Nanocomposites. *Polym. Compos.* **2012**, *33* (10), 1672−1677.
(49) Garcia-Muñoz, P.; Fresno, F.; de la Peña O'Shea, V. A.; Keller, N. Ferrite Materials for Photoassisted Environmental and Solar Fuels Applications. *Top. Curr. Chem.* **2020**, *378* (1), 378.
(50) Taffa, D. H.; Dillert, R.; Ulpe, A. C.; Bauerfeind, K. C. L.; Bredow, T.; Bahnemann, D. W.; Wark, M. Photoelectrochemical and Theoretical Investigations of Spinel Type Ferrites ($M_xFe_{3-x}O_4$) for Water Splitting: A Mini-Review. *J. Photonics Energy* **2017**, *7* (1), 012009.
(51) Delli Pizzi, A.; Basilico, R.; Cianci, R.; Seccia, B.; Timpani, M.; Tavoletta, A.; Caposiena, D.; Faricelli, B.; Gabrielli, D.; Caulo, M. Rectal Cancer MRI: Protocols, Signs and Future Perspectives Radiologists Should Consider in Everyday Clinical Practice. *Insights Imaging* **2018**, *9* (4), 405−412.

(52) Zhu, X.; Guijarro, N.; Liu, Y.; Schouwink, P.; Wells, R. A.; Le Formal, F.; Sun, S.; Gao, C.; Sivula, K. Spinel Structural Disorder Influences Solar-Water-Splitting Performance of $ZnFe_2O_4$ Nanorod Photoanodes. *Adv. Mater.* **2018**, *30* (34), 1801612.
(53) Kaneko, H.; Kodama, T.; Gokon, N.; Tamaura, Y.; Lovegrove, K.; Luzzi, A. Decomposition of Zn-Ferrite for O_2 Generation by Concentrated Solar Radiation. *Sol. Energy* **2004**, *76* (1−3), 317−322.
(54) Kaneko, H.; Gokon, N.; Hasegawa, N.; Tamaura, Y. Solar Thermochemical Process for Hydrogen Production Using Ferrites. *Energy* **2005**, *30*, 2171−2178.
(55) Takahashi, Y.; Aoki, H.; Kaneko, H.; Hasegawa, N.; Suzuki, A.; Tamaura, Y. Oxygen-Gas-Releasing Reaction of Zn Ferrite by Xe Lamp Beam Irradiation in Air at 1800 K. *Solid State Ionics* **2004**, *172* (1−4), 89−91.
(56) Tamaura, Y.; Kaneko, H. Oxygen-Releasing Step of $ZnFe_2O_4$/(ZnO + Fe_3O_4)-System in Air Using Concentrated Solar Energy for Solar Hydrogen Production. *Sol. Energy* **2005**, *78* (5), 616−622.
(57) Kaneko, H. Water Splitting by Using a Metal Oxide for Solar Thermal/Chemical Energy Conversion. *Eco-Engineering* **2002**, *14* (4), 3−9.
(58) Fan, X.; Liu, Y.; Chen, S.; Shi, J.; Wang, J.; Fan, A.; Zan, W.; Li, S.; Goddard, W. A.; Zhang, X. M. Defect-Enriched Iron Fluoride-Oxide Nanoporous Thin Films Bifunctional Catalyst for Water Splitting. *Nat. Commun.* **2018**, *9* (1), 1−11.
(59) Philip, J.; Gnanaprakash, G.; Panneerselvam, G.; Antony, M. P.; Jayakumar, T.; Raj, B. Effect of Thermal Annealing under Vacuum on the Crystal Structure, Size, and Magnetic Properties of $ZnFe_2O_4$ Nanoparticles. *J. Appl. Phys.* **2007**, *102* (5), 054305.
(60) Ayyappan, S.; Paneerselvam, G.; Antony, M. P.; Philip, J. Structural Stability of $ZnFe_2O_4$ Nanoparticles under Different Annealing Conditions. *Mater. Chem. Phys.* **2011**, *128* (3), 400−404.
(61) Dolcet, P.; Diodati, S.; Zorzi, F.; Voepel, P.; Seitz, C.; Smarsly, B. M.; Mascotto, S.; Nestola, F.; Gross, S. Very Fast Crystallisation of MFe_2O_4 Spinel Ferrites (M = Co, Mn, Ni, Zn) under Low Temperature Hydrothermal Conditions: A Time-Resolved Structural Investigation. *Green Chem.* **2018**, *20* (10), 2257−2268.
(62) Nordhei, C.; Ramstad, A. L.; Nicholson, D. G. Nanophase Cobalt, Nickel and Zinc Ferrites: Synchrotron XAS Study on the Crystallite Size Dependence of Metal Distribution. *Phys. Chem. Chem. Phys.* **2008**, *10* (7), 1053−1066.
(63) Sikora, M.; Kapusta, C. Z.; Zajac, D.; Tokarz, W.; Attenkofer, K.; Fischer, P.; Goering, E.; Schütz, G. X-MCD Study of Mixed Valence Manganites. *J. Alloys Compd.* **2001**, *328* (1−2), 100−104.
(64) Glatzel, P.; Sikora, M.; Smolentsev, G.; Fernández-García, M. Hard X-Ray Photon-in Photon-out Spectroscopy. *Catal. Today* **2009**, *145* (3−4), 294−299.
(65) Daffé, N.; Sikora, M.; Rovezzi, M.; Bouldi, N.; Gavrilov, V.; Neveu, S.; Choueikani, F.; Ohresser, P.; Dupuis, V.; Taverna, D.; Gloter, A.; Arrio, M. A.; Sainctavit, P.; Juhin, A. Nanoscale Distribution of Magnetic Anisotropies in Bimagnetic Soft Core-Hard Shell $MnFe_2O_4$@$CoFe_2O_4$ Nanoparticles. *Adv. Mater. Interfaces* **2017**, *4* (22), 1700599.
(66) Szczerba, W.; Costo, R.; Veintemillas-Verdaguer, S.; Del Puerto Morales, M.; Thünemann, A. F. SAXS Analysis of Single-and Multi-Core Iron Oxide Magnetic Nanoparticles. *J. Appl. Crystallogr.* **2017**, *50*, 481−488.
(67) Piquer, C.; Laguna-Marco, M. A.; Roca, A. G.; Boada, R.; Guglieri, C.; Chaboy, J. Fe K-Edge X-Ray Absorption Spectroscopy Study of Nanosized Nominal Magnetite. *J. Phys. Chem. C* **2014**, *118* (2), 1332−1346.
(68) Upadhyay, C.; Verma, H. C.; Sathe, V.; Pimpale, A. V. Effect of Size and Synthesis Route on the Magnetic Properties of Chemically Prepared Nanosize $ZnFe_2O_4$. *J. Magn. Magn. Mater.* **2007**, *312* (2), 271−279.
(69) Ravel, B.; Newville, M. ATHENA, ARTEMIS, HEPHAESTUS: Data Analysis for X-Ray Absorption Spectroscopy Using IFEFFIT. *J. Synchrotron Radiat.* **2005**, *12* (4), 537−541.
(70) Gilliland, S. E.; Carpenter, E. E.; Shultz, M. D. Modified Seed Growth of Iron Oxide Nanoparticles in Benzyl Alcohol — Optimization for Heating and Broad Stability in Biomedical Applications. *Nanobiomedicine* **2014**, *1*, 9.
(71) Kocjan, A.; Logar, M.; Shen, Z. The Agglomeration, Coalescence and Sliding of Nanoparticles, Leading to the Rapid Sintering of Zirconia Nanoceramics. *Sci. Rep.* **2017**, *7*, 2541.
(72) Aqzna, S. S.; Yeoh, C. K.; Supri, A. G.; Atiqah, T. N.; Amali, H. K.; Khalijah, S. K.; Aw, Y. Y.; Teh, P. L. Effect of Stoichiometry and Sintering Temperature on the Mechanical Properties of Zinc Ferrite ($Zn_xFe_{3-x}O_4$). *Mater. Sci. Forum* **2016**, *857*, 126−130.
(73) Dippong, T.; Deac, I. G.; Lazar, M. D.; Petean, I.; Levei, E. A.; Borodi, G.; Cadar, O. Effect of Heat-Treatment Temperature and Zinc Addition on Magnetostructural and Surface Properties of Manganese Nanoferrite Prepared by an Ecofriendly Sol-Gel Synthesis. *J. Mater. Res. Technol.* **2021**, *15*, 6528−6540.
(74) Goya, G. F.; Rechenberg, H. R.; Chen, M.; Yelon, W. B. Magnetic Irreversibility in Ultrafine $ZnFe_2O_4$ Particles. *J. Appl. Phys.* **2000**, *87* (11), 8005−8007.
(75) Hofmann, M.; Campbell, S. J.; Ehrhardt, H.; Feyerherm, R. The Magnetic Behaviour of Nanostructured Zinc Ferrite. *J. Mater. Sci.* **2004**, *39* (16−17), 5057−5065.
(76) Özdemir, Ö.; Dunlop, D. J. Hysteresis and Coercivity of Hematite. *J. Geophys. Res. Solid Earth* **2014**, *119* (4), 2582−2594.
(77) Hölscher, J.; Petrecca, M.; Albino, M.; Garbus, P. G.; Saura-Múzquiz, M.; Sangregorio, C.; Christensen, M. Magnetic Property Enhancement of Spinel Mn-Zn Ferrite through Atomic Structure Control. *Inorg. Chem.* **2020**, *59* (15), 11184−11192.
(78) Stewart, S. J.; Figueroa, S. J. A.; Ramallo López, J. M.; Marchetti, S. G.; Bengoa, J. F.; Prado, R. J.; Requejo, F. G. Cationic Exchange in Nanosized $ZnFe_2O_4$ Spinel Revealed by Experimental and Simulated Near-Edge Absorption Structure. *Phys. Rev. B - Condens. Matter Mater. Phys.* **2007**, *75* (7), 1−5.
(79) Klementiev, K.; Chernikov, R. XAFSmass: A Program for Calculating the Optimal Mass of XAFS Samples. *J. Phys. Conf. Ser.* **2016**, *712* (1), 012008.
(80) Frazer, B. H.; Gilbert, B.; Sonderegger, B. R.; De Stasio, G. The Probing Depth of Total Electron Yield in the Sub-KeV Range: TEY-XAS and X-PEEM. *Surf. Sci.* **2003**, *537* (1−3), 161−167.

https://doi.org/10.1021/acs.iecr.2c01572
Ind. Eng. Chem. Res. 2022, 61, 12532−12544